Progress in Natural Science: Materials International 34 (2024) 1281–1294

HOSTED BY

ELSEVIER

Contents lists available at ScienceDirect

Progress in Natural Science: Materials International

journal homepage: www.elsevier.com/locate/pnsmi

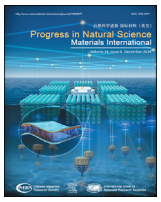

Synthesis of lignite-derived carbon materials for fast sodium-ion storage in a wide temperature range by ultrafast Joule heating

Ru Wang [a], Yiming Fan [c], Jiaqi Wang [b], Yuyang Li [d], Xiangyang Li [e], Feng Jin [c,**], Xiaofei Hu [a,*]

[a] School of Chemistry, Engineering Research Center of Energy Storage Materials and Devices, Ministry of Education, State Key Laboratory for Mechanical Behavior of Materials. Xi'an Jiaotong University, Xi'an, 710049, Shaanxi, PR China
[b] Department of Chemistry and Biochemistry. Northern Illinois University, DeKalb, IL, 60115, USA
[c] State Key Laboratory for Strength and Vibration of Mechanical Structures, Xi'an Jiaotong University, Xi'an, 710049, Shaanxi, PR China
[d] State Key Laboratory of Electrical Insulation and Power Equipment, School of Electrical Engineering, Xi'an Jiaotong University, Xi'an, Shaanxi, 710049, PR China
[e] Xi'an Institute of Electromechanical Information Technology, Xi'an, 710065, PR China

ARTICLE INFO

Keywords:
Sodium-ion batteries
High-rate
Lignite
High-temperature thermal shock pulse
A wide temperature range

ABSTRACT

The advancement of sodium-ion batteries is hindered by the imperative to reconcile extreme environmental conditions and high-rate demands, posing challenges in the synthesis of cost-effective and high-performance anode materials. Among the potential candidates, lignite-based soft carbon materials stand out due to their abundant resources and low cost. An ultrafast approach using high-temperature thermal shock pulses is reported for the synthesis of soft carbon anode from lignite, and the mechanism of "adsorption-intercalation-pore filling" is proposed. Based on structure analysis, in/ex-situ electrochemically characterization, and calculation/simulation, high concentration of defects and C=O contents, along with abundant closed pore structures, contribute to enhancing the sodium storage capabilities of the material. The optimized sample demonstrates a substantial reversible capacity of 300.6 mAh g^{-1} at 0.1C and outstanding high-rate capability at 10.0C, which also maintains proper functionality in a wide temperature range (−40~80 °C). This performance surpasses that of previously reported lignite-based soft carbon materials. Additionally, the assembled full-cell maintains a high-energy density of 235.8 Wh kg^{-1}. This work provides valuable insights into developing anode materials for coal-based SIBs at high-rate current densities in a wide range of temperatures.

1. Introduction

Sodium-ion batteries (SIBs) are considered as an ideal type of electrochemical energy storage system due to their cost-effectiveness and the abundant sodium resources [1–5]. The large-scale application of SIBs undoubtedly hinges on the development of high-performance electrode materials [6–11]. Coal-derived soft carbon materials have been investigated as potential SIB anodes due to their widespread geographical distribution and cost advantages [12–14]. Hu et al. pioneered reported anthracite-based SIB anodes achieved a reversible capacity of 222 mAh g^{-1} at 0.1C, and passed the safety test without catching fire, suggesting the utilization potentiality [15]. Zhao et al. proposed a thermal conversion pathway to create closed pores and enhance the sodium storage capacity of anthracite-based soft carbon with an excellent reversible capacity of 308 mAh g^{-1} at 0.1C and a rate performance of 86.4 mAh g^{-1} at 2.0C [16]. Despite these advancements, the sodium storage capacity and rate performance of these anthracite-derived carbon anode materials and the relatively high cost of anthracite are still considered unsatisfactory for practical application in SIBs. Therefore, further research and development is necessary to enhance their commercial viability.

Various strategies have been explored to improve the rate performance of coal-based carbon anodes, including porous structure design, heteroatom doped, and surface modification [17–19]. Qiu et al. achieved a hierarchical pore structure through a solvent extraction approach in bituminous-based soft carbon material [20]. The pore-modified coal--based electrodes allowed an excellent rate capacity of 79 mAh g^{-1} at 10 A g^{-1}. To further search for SIB anodes with cost advantages, Li et al. investigated the differences in sodium storage performance among three representative metamorphic-grade coals [21]. After oxygen functionalization of the precursor materials, the lignite-derived soft carbon with a

* Corresponding author.
** Corresponding author.
E-mail addresses: jinfengzhao@263.net (F. Jin), xiaofei.hu@xjtu.edu.cn (X. Hu).

https://doi.org/10.1016/j.pnsc.2024.11.002
Received 8 August 2024; Received in revised form 29 October 2024; Accepted 3 November 2024
Available online 10 December 2024

high content of defects and oxygen functional groups exhibited an outstanding reversible capacity of 162.4 mAh g^{-1} at 1 A g^{-1}. Meanwhile, Xu et al. synthesized a lignite-based SIB anode with a reversible capacity of 106.1 mAh g^{-1} at 1 A g^{-1} by pitch vapor deposition strategy [22]. The above researches show that lignite with low cost can be regarded as a potential SIB anode. However, traditional methods for preparing lignite-based carbon anode materials for SIBs typically involve tube furnace annealing (TFA), which requires heating for 2 h or more, with relatively slow heating and cooling rates, resulting in a prolonged preparation cycle and low efficiency. Therefore, a rapid and efficient preparation process for SIB carbon materials is imperative [23–25]. Moreover, while most researches concentrate solely on the room temperature performance of SIBs, further exploration under a wide temperature range is essential to diversify the application scenarios. Up to now, there are no reports about coal-based soft carbon SIB anodes with a high capacity, decent rate performance, and long cycle stability simultaneously in a wide temperature range.

Inspired by previous research, we herein report a rapid and efficient method called high-temperature thermal shock pulse (HTSP) that prepares carbon anode for SIBs using lignite as the raw material. The optimized lignite-based SIB anode with high concentration of defects and C=O contents, along with abundant closed pore structures, exhibits fast Na^+ diffusion and electron transfer capabilities. Its exceptional desolvation ability promotes the electrochemical reaction rate of Na^+ at the electrode interface. Simultaneously, the stable solid electrolyte interface (SEI) induces uniform sodium deposition and effectively inhibits the formation of sodium dendrites. Therefore, the LC-1400 °C electrode exhibits exceptional electrochemical performance with a high sodium storage capacity at 0.1C (176.2 mAh g^{-1}@-40 °C, 300.6 mAh g^{-1}@25 °C, 706.8 mAh g^{-1}@80 °C) and outstanding rate performance at 5.0C in a wide range temperature (71.7 mAh g^{-1}@-20 °C, 205.4 mAh g^{-1}@25 °C and 62.2 mAh g^{-1}@60 °C), surpassing that of commercial soft carbon. More importantly, a full battery constructed by using the LC-1400 °C electrode as the anode and paired it with the commercial $Na_3V_2(PO_4)_3$ (NVP) cathode also exhibits exceptional long-cycle capacity (103.9 mAh g^{-1} at 1.0C with a capacity retention of 91.3 % over 500 cycles and 86.1 mAh g^{-1} at 5.0C with a capacity retention of 86.5 % over 350 cycles at 25 °C) and decent high-rate performance at both room temperature (70.5 mAh g^{-1}@10.0C) and low-temperature (35.2 mAh g^{-1}@2.0C). The assembled pouch cell can light LED bulbs under normal conditions, withstand nail penetration, and even endure being cut into pieces. This work highlights the enormous potential of employing the HTSP approach to prepare high-performance soft carbon for SIBs.

2. Materials and methods

2.1. Material synthesis

The bulk lignite and anthracite obtained from Nei Mongol of China. The commercial soft carbon, graphite, and pitch was purchased from Si Chuan Best Graphite New Energy Corp, Shen Zhen Btr New Energy Materials Co., Ltd, and Shen Zhen Kejing star technology company, respectively. The precursor of biomass-derived carbon was wood.

The lignite-derived carbon was prepared by a two-step method. The first step was to get the lignite precursors. Typically, the bulk lignite was smashed to obtain powers. Then the powers were added into the mixed solution of HF and HCl (vol. ratio 1:3) under magnetic stirring at room temperature for 12 h to remove the ash, and then multiple washing with deionized water until neutral. The targeted precursors were acquired after drying overnight at 100 °C. The second step was to fabricate lignite-derived carbon for sodium-ion battery anode materials. The whole High-temperature thermal shock pulse (HTSP) based on the principle of Joule heating proceeded in an Ar-filled acrylic box. According to controlling direct current power supply, the materials could reach high temperatures in an instant. The time-temperature curve was recorded by the high-temperature infrared thermometer. Carbon cloth was linked to copper clips as a conductive substrate. The precursor powers were laid on the interlayer of the carbon cloth to prevent the powder from falling during high-temperature heat treatment. Fixed the number of pulses and adjusted different currents and voltages, three lignite-derived carbon materials were obtained. The prepared carbons were denoted as the LC-1200 °C, the LC-1400 °C, and the LC-1550 °C, respectively. Similarly, the biomass/pitch/anthracite-derived carbon materials were obtained by HTSP at 1400 °C.

2.2. Material characterization

The morphologies and nanostructures of the lignite-derived carbon materials were characterized by Scanning electron microscopy (SEM, GeminiSEM 500) and transmission electron microscopy (TEM, JEM—F200 FEI Tecnai G2 F20 FEI Talos F200s). The surface potential and roughness of the prepared materials are analyzed by atomic force microscope (AFM, Bruker Dimension Icon). The amorphous structure of the samples was implemented by X-ray diffraction patterns (XRD, BURKER D2-phaser) with Cu Kα radiation (λ = 0.15406 nm). The graphitization degree of the carbon materials was determined by Raman spectroscopy (Raman, Renishaw inVia) using a 633 nm laser. The chemical composition and contents on the surface of the samples were tested by X-ray photoelectron spectrometer (XPS, ESCALAB Xi+). The carbon content of the raw lignite was performed by thermal gravimetric analysis (TGA, TA-SDT650) from 30 °C to 1200 °C at a heating rate of 10 °C min^{-1} under the Ar atmosphere. The specific surface area and the pore size distribution were examined by N_2 adsorption/desorption (Micromeritics ASAP 2460). The true density of the three carbon materials was investigated by the True density analyzer (Accupyc II 1345). The electrical conductivity of the carbon materials was calculated by the Resistivity tester (ST2253y). The closed pore characteristic of the samples was measured by small angle X-ray scattering (SAXS, xenocs-xeuss 2.0). The oxygen function groups' distribution of the samples was recorded by Thermogravimetric mass spectrometer (TG-MS, TA Instruments, SDT 650+Discovery MS).

2.3. Electrochemical measurements

All the electrochemical tests used CR2023 coin cells and the battery assembly process was carried out in a glove box filled with argon gas. The lignite-derived carbon was mixed with Super P and polyvinylidene fluoride (PVDF) binder in a weight ratio of 8:1:1 and evenly dispersed in N-methyl pyrrolidone (NMP) solvent. After manual grinding for a few minutes, the uniform slurry was scraped on the aluminum foil current collector and then dried in a vacuum oven at 100 °C for 12 h. The electrodes were cut into a circle with a radius of 6 mm and the mass loading of active material was about 1.3–1.6 mg cm^{-2}. For the half-cell test, metal sodium was used as counter electrodes, a glass fiber (GF/D, Whatman) was used as the separator, and 1M $NaPF_6$ (diglyme) as the electrolyte. In order to compare the performance differences of LC-1400 °C in ether and ester electrolyte, 1M $NaPF_6$ in EC and DMC (1:1 in volume) as an ester electrolyte. For the full-cell test, commercial $Na_3V_2(PO_4)_3$(NVP) as cathode, NVP was mixed with Super P and PVDF in a ratio of 8:1:1 and the mass loading of NVP was about 3.5–4 mg cm^{-2}, LC-1400 °C and commercial soft hard as anode, respectively. The capacity of the full battery was calculated based on the cathode weight loading. Electrochemical performance tests using Neware battery testers were performed in a voltage range of 0.01V–3.0 V for half battery and 2.0–3.8 V for the full battery. The cyclic voltammetry (CV) was characterized by the CHI660E electrochemistry workstation at different scan rates. The EIS curves were recorded in the frequency range from 1 mHz to 100 kHz.

2.4. Computational method

All electronic structure calculations are performed using the ORCA (version 5.0.4) software package. ORCA is a versatile quantum chemistry

program capable of performing various types of calculations, including density functional theory (DFT), Hartree-Fock (HF), and post-HF methods. Geometry optimizations are carried out using the B97-3C functional with the embedded basis set. Single-point energy calculations are performed using the RI-B3LYP-D3(BJ) function with the larger def2-TZVP basis set to obtain accurate electronic energies. To account for dispersion interactions, the DFT-D3 correlation correction is included in the calculations. This correction accounts for the long-range dispersion forces that are not adequately captured by standard DFT functionals. The D3 correction was applied with the Becke-Johnson damping scheme.

2.5. COMSOL multiphysics simulation

The framework of this electrochemical model is established based on the Newman battery model. All the numerical simulation is performed using COMSOL Multiphysics software. The electrochemical parameters and material parameters in the model are set to be consistent with the experimental results (parameters such as equilibrium potential, diffusion coefficient, and so on are derived from experimental test data). In addition, it should be noted that in the preparation process, the actual electrode can't guarantee the uniform distribution of active particles. We calculated the average particle size based on the SEM characterization results of the material as the value used in the model. The C-rate of the simulation is 5.0C (current density is 17.684 A/m^2), and the temperature is 298 K.

3. Results and discussion

3.1. Screen preparation device and precursor

This method involves acid washing and a HTSP carbonization process. The HTSP method based on electrical Joule heating technology offers heightened flexibility and controllability, enabling rapid heating of carbon materials to high temperatures in a short timeframe. Additionally, the accelerated cooling rate associated with the HTSP method allows for precise control over the structure and properties of the material. Adjusting the preparation conditions, not only shortens the cycle time and improves efficiency but also yields carbon anode materials with excellent electrochemical properties. The optimization of preparation devices holds significant importance in enhancing the overall performance of the SIBs and reducing energy consumption. Fig. 1a illustrates a comparison between two methods for preparing carbon anodes for SIBs. The HTSP is proven to be advantageous over TFA due to its faster processing times and more efficient preparation of carbon materials. The adoption of HTSP can significantly shorten the entire process duration to approximately 2 min with rapid heating (~370 K/s) and fast cooling (~100 K/s) rates (Fig. 1b). Moreover, selecting the appropriate carbon precursors is also vital in achieving the desired properties. In this study, six different carbon precursors are evaluated, and lignite is identified as a cost-effective option with relatively abundant reserves and widespread distribution (Fig. 1c and Table S1). Simultaneously, the initial charge capacity of lignite-based derived soft hard can be comparable to the hard carbon derived from biomass and has the highest initial coulombic efficiency (Fig. 1d). The rate performance of the six samples is measured at various current densities from 0.1 to 5.0C (1.0C = 300 mA g^{-1}) (Fig. 1e). Compared to the other five kinds of carbon materials, the lignite-derived soft carbon electrode exhibits ultrahigh rate performance with a reversible capacity of 205.4 mAh g^{-1} at 5.0C. Therefore, the successful synthesis of high-rate performance lignite-based carbon anode materials using HTSP is achieved.

3.2. Wide temperature range performance

Many researches have shown that the solvation structure and interface behavior of ions play a crucial role in battery performance. Evaluating the charge transfer rate depends on the desolvation ability of Na^+ (Fig. 2a). The LC-1400 °C electrode contains a higher concentration of defects and C=O compared to the commercially soft carbon (CSC) electrode (Fig. S1 and Table S2). Consequently, the LC-1400 °C electrode exhibits a rapid desolvation ability due to the strong interaction between

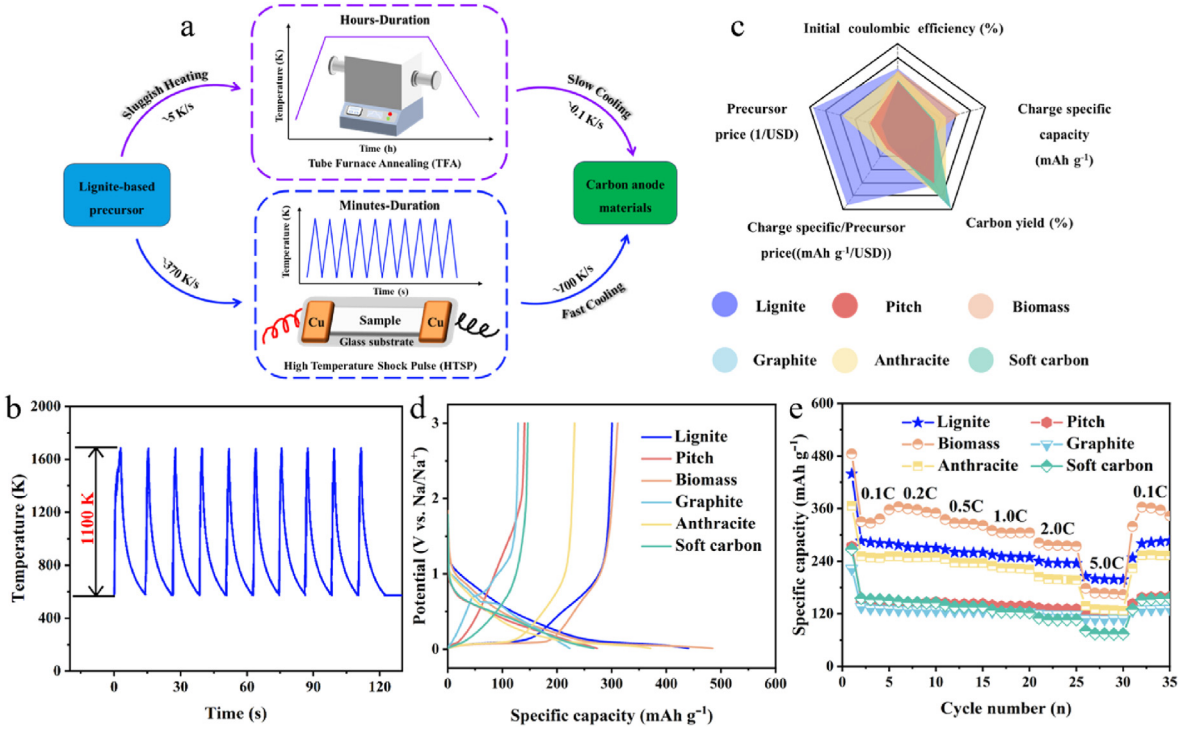

Fig. 1. (a) Schematic illustration comparison between the HTSP method and TFA approach for synthesizing Lignite-based carbon sodium-ion batteries soft anode. (b) Temperature-Time curve of the HTSP process. (c) The radar plot compares different carbon precursors. (d, e) Comparison of half-cell electrochemical performance for different carbon precursors. (d) Galvanostatic charge/discharge (GCD) profiles at a current density of 0.1C. (e) Rate capability at different current densities.

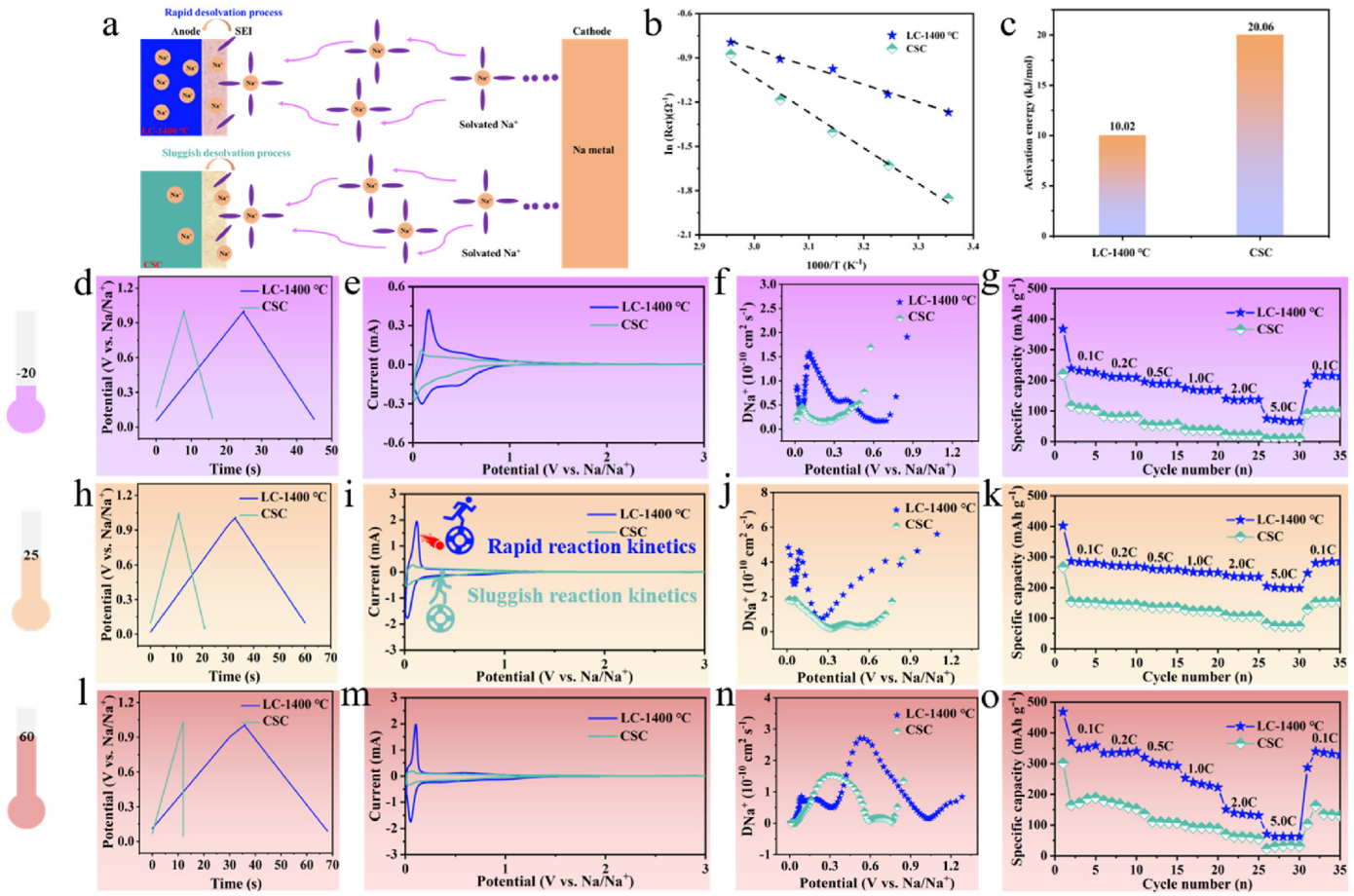

Fig. 2. (a) Schematic illustrations of the Na^+ migration behaviors at different carbon substrates. (b–c) The activation energies of the LC-1400 °C electrode and the CSC electrode by fitting EIS dates in various temperatures. (d–o) Comparison of half-cell electrochemical performance between the LC-1400 °C electrode and the CSC electrode in a wide temperature range. Desolvation ability (d–l). CV curves at 0.2 mV s^{-1} (e–m). The Na^+ diffusion coefficient during the discharge process (f–n). Rate capability (g–o).

defects/C=O and Na^+, therefore accelerating uniform sodium deposition and improving the interfacial ion diffusion and reaction kinetics [26,27]. We also demonstrate the desolvation ability of the two electrode materials at different temperatures from the experiment aspect (Fig. 2b–c and 2d-2l). The activation energy (Ea) for the charge transfer impedance of Na^+ on the surface of the two different anode carbon electrodes is determined by fitting the variable temperature impedance. The LC-1400 °C electrode possesses a lower Ea and longer charge/discharge time than the CSC electrode, revealing that the LC-1400 °C electrode has a lower desolvation barrier and faster kinetics for Na^+ compared to the CSC electrode [28]. Using Cyclic Voltammetry (CV) curves (Fig. 2e-m, and Fig. S2) and Electrochemical Impedance Spectroscopy (EIS) (Fig. S3), we can observe the electrochemical behavior of the two materials at temperatures ranging from −20 to 80 °C. The CV curves of the CSC electrode almost lack sharp redox peaks, indicating that the sodium storage sites are mainly provided by the slope region. This leads to a notable decrease in overall sodium storage capacity, as observed in the discharge curves in Fig. 1d. Fig. S3 displays the EIS curves of the two carbon materials from −20 to 80 °C. All EIS curves include a semicircle related to the charge transfer (Rct) and a slope line dependent on Warburg diffusion resistance (W). According to Nyquist plots, the LC-1400 °C electrode has a lower Rct value and high W slope compared to the CSC electrode, demonstrating superior fast ion and electronic transport kinetics. The Galvanostatic Intermittent Titration technique (GITT) is used to study the diffusivity coefficient of Na^+ with rest intervals for 1 h and a pulse current for 10 min at 0.1C (Fig. 2f-n, and Fig. S_4-S_6). The sodium diffusion trend of the LC-1400 °C electrode and CSC electrode in the slope region is consistent, indicating that they have similar sodium storage mechanisms in the high voltage range at varied temperatures. Meanwhile, the LC-1400 °C electrode exhibits a higher D_{Na}^{+} during the charge and discharge process due to faster reaction kinetics originating from the higher concentration of defects and oxygen-containing functional groups in the intrinsic materials. Thanks to its unique carbon structure and fast sodium storage capacity, the LC-1400 °C electrode has exceptional excellent performance in wide range of temperatures (Fig. 2g-o, and Figs. S7–S9). Moreover, the LC-1400 °C electrode displays excellent high-rate performance from −20 to 60 °C (Fig. 2g-o and Fig. S10). At a current density of 5.0C, the reversible capacity of the LC-1400 °C electrode is as follows: 71.7 mAh g^{-1}@-20 °C, 100.8 mAh g^{-1}@0 °C, 205.4 mAh g^{-1}@25 °C, 176.7 mAh g^{-1}@40 °C and 62.2 mAh g^{-1}@60 °C. In contrast, the CSC electrode only achieves a reversible capacity of 9.1 mAh g^{-1}@-20 °C, 40.8 mAh g^{-1}@0 °C, 74.2 mAh g^{-1}@25 °C, 123.3 mAh g^{-1}@40 °C, 32.5 mAh g^{-1}@60 °C. Finally, the performance of the LC-1400 °C electrode is tested under extreme conditions (Fig. S11). After cycling at −20 °C with a current density of 0.1C for 20 cycles, the electrode is brought to room temperature and cycle at 1.0C. The capacity retention is 93.4 % compared to direct cycling at room temperature, providing further confirmation of the excellent electrochemical performance of the lignite-derived carbon anode.

3.3. Mechanism analysis

From the above studies, it is evident that the interaction of oxygen-containing functional groups on Na^+ significantly affects the battery

performance. We conduct a comparison between our prepared material and CSC on the influence of oxygen-containing functional groups on Na^+ adsorption. Density functional theory (DFT) calculations are employed to examine the impact of three oxygen functional groups containing COOH, C-O-C, and C=O (Fig. 3a–b). It is found that the adsorption energies (ΔEa) of the C=O are higher than COOH and C-O-C, indicating that C=O has the strongest adsorption capacity for Na^+. Additionally, the LC-1400 °C electrode, which contains a higher proportion of C=O than the CSC electrode, offers more sodium adsorption sites. This feature is advantageous for improving sodium storage performance. To further explore the differences in performance between the LC-1400 °C electrode and the CSC electrode at different temperatures, we thermodynamically correct and test the adsorption free energy at −20, 25, and 60 °C, as shown in Fig. 3c–e. Results evidence that the LC-1400 °C electrode exhibits higher adsorption-free energy at the three temperatures, with C=O being the main functional group responsible for Na^+ adsorption. As the temperature increases, the adsorption-free energy of the oxygen-containing functional groups in both materials decreases, likely due to the increase in system entropy and the accompanying tendency towards disorder. This resulted in more intense movement of Na^+ and electrode materials, ultimately offsetting the original chemical bond strength. The discrepancy of sodium deposition behavior on the surface of the LC-1400 °C electrode and the CSC electrode is further observed by in-situ optical microscope at a high current density of 2.5 mA cm^{-2} (Fig. 3f and g). The LC-1400 °C electrode, with its high ionic diffusion coefficient, facilitates the entry of Na^+ into the bulk materials through the interface instead of plating on the surface. As shown in Fig. 3f, a small amount of sodium appears on the surface of the LC-1400 °C electrode after approximately 13 min, and its surface remains uniformly thick in the subsequent deposition process without the formation of Na dendrite and bubbles. In contrast, after about 4.5 min, the surface of the CSC electrode generates numerous randomly distributed Na protrusions (Fig. 3g). Due to the uneven Na nucleation, a plentiful of bubbles and dendrites form throughout the deposition process. This observation highlights the advantages of the LC-1400 °C electrode in regulating sodium deposition and its potential as a fast-charging material for SIBs.

COMSOL Multiphysics software is employed for numerical simulation to further investigate the phenomenon of sodium deposition on the electrode surface during fast charge. While the experimental observation reveals that the deposited sodium exhibits a complex mossy morphology, our main focus in this study is not to accurately simulate the morphology. Instead, the purpose of the simulation is to provide another perspective to demonstrate the superiority of the LC-1400 °C electrode. To simplify the simulation, we defined a small rectangular area as a "sodium dendrite". The framework of this electrochemical model is established based on the theory, namely the Newman battery model [29]. The detailed methodology for the simulation can be found in the COMSOL Multiphysics simulation.

The results of the numerical simulation are plotted in Fig. 3h. For the CSC electrode material, sodium deposition occurs at 160s, while for the LC-1400 °C electrode, the deposition phenomenon is significantly delayed and occurs at 490s. To analyze the discharge of electrolyte salt at different discharge stages, we select three points and create the sodium ion concentration distribution cloud map in the electrolyte. The arrows

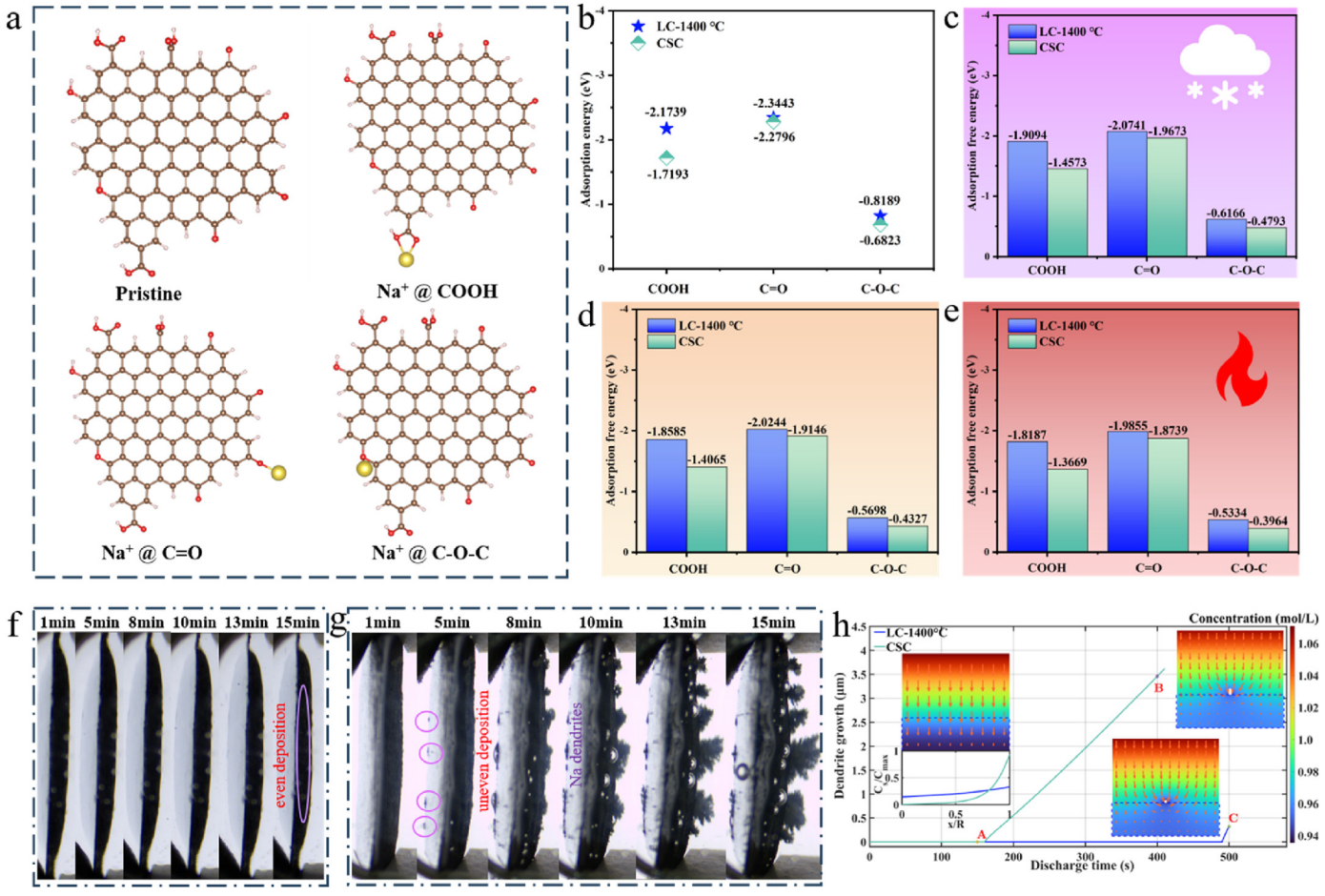

Fig. 3. (a) Simulation and different oxygen groups adsorption site of Na^+. Comparison of adsorption energy (b) and adsorption free energy (c–e) between the LC-1400 °C electrode (a) and the CSC electrode. In situ optical microscope of the LC-1400 °C electrode (f) and the CSC electrode (g). (h) COMSOL model of the LC-1400 °C electrode and the CSC electrode.

on the map represent the sodium ion flux in the electrolyte, and the length of the arrows reflects the relative magnitude of flux at that point. The blue dashed box represents the electrode area, and the white rectangle represents the "sodium dendrite". When the discharge state is at point A, neither the CSC electrode nor the LC-1400 °C electrode has undergone sodium deposition. At this time, sodium ions in the electrolyte start from the metal electrode side, pass through the separator/electrolyte and enter the soft carbon electrode for insertion reaction. The sodium ion flux is largest near the separator side surface, gradually decreasing as it approaches the collectors until it reaches 0, aligning with the physical observation. At point B, sodium deposition initiates on the surface of the CSC electrode. Sodium ions in the electrolyte rush towards the metal sodium, and the deposition reaction persists, exhibiting a marked contrast to the state observed at point A. At Point C, sodium deposition initiates on the surface of the LC-1400 °C electrode. The simulated discharge time is set to 500 s in total, unlike the CSC electrode, at the end of discharge, only a minimal amount of sodium deposition is observed on the surface of the LC-1400 °C electrode. Overall, these simulations provide valuable insights into the sodium deposition phenomenon and highlight the advantages of the LC-1400 °C electrode material in delaying and reducing sodium deposition.

Based on the characterization data of the materials, we have provided a theoretical explanation for both the experimental and simulation results. The conclusion drawn is that the LC-1400 °C electrode material has a lower tendency for sodium deposition compared to the CSC electrode material, attributed to its higher solid diffusion coefficient.

$$\begin{cases} \dfrac{\partial C_s}{\partial t} + \nabla \cdot \mathbf{J}_s = 0 \\ \mathbf{J}_s = -D_s(\nabla C_s) \end{cases} \tag{1}$$

The diffusion of sodium ions in the active material is regulated by the diffusion equation, where C_s represents the sodium ion concentration in the active particles, D_s is the diffusion coefficient of sodium ions in the electrode particles, and $\mathbf{J}_s$ denotes the sodium ion flux.

When the solid diffusion rate is slower than the intercalation reaction, the surface of the active particles becomes crowded. Once the surface of the active particles reaches saturation ($C_s \rightarrow C_{max}$), the intercalation reaction rate significantly decreases, resulting in the applied current promoting the formation of sodium metal and subsequent sodium plating. Referring to the research of Gao et al. [30], the time scale of the diffusion process is:

$$\tau_D = \frac{R^2}{D_s} \tag{2}$$

Where R represents the diffusion characteristic length (related to particle size). This time scale needs to be compared with the time scale of sodium, and the smaller the τ_D value, the lesser the chance of sodium plating occurrence.

According to the experimental results, the diffusion coefficient of the LC-1400 °C electrode is approximately one order of magnitude higher than that of the CSC electrode. The particle sizes used in the simulation for both electrode materials are similar (around 10 μm according to SEM results, as shown in Fig. S12). Consequently, the characteristic diffusion time of sodium ions in the LC-1400 °C electrode is approximately one order of magnitude shorter than that in the CSC electrode. This conclusion sheds light on the superior performance of the LC-1400 °C electrode. Gao et al. also emphasize that $C_s/C_{max} \rightarrow 1$ (at the particle surface) fulfills the condition for sodium plating occurrence. The concentration distribution of sodium ions is studied in the active particle on the upper surface of the electrode when the discharge state is at point A. A normalized concentration curve (C_s/C_{max}) is plotted, with the abscissa representing the normalized distance from the particle center. As shown in Fig. 3h, for the LC-1400 °C electrode, there is a small difference in sodium ion concentration between the particle surface and the particle center, resulting in a relatively flat concentration distribution curve along the radial direction of the particle. The concentration at the particle surface deviates significantly from 1. On the contrary, for the CSC electrode, the concentration gradient of sodium ions within the particle is large, and the concentration on the particle surface approaches 1. Simulation results indicate that for CSC materials, sodium deposition occurs immediately after point A, which aligns perfectly with the theory proposed by Gao et al. [30].

3.4. Features of prepared lignite-derived soft carbon

Lignite is a low-grade mineral coal with high ash contents. The preparation of high-performance lignite-based SIBs soft anode is built upon acid washing and high-temperature carbonization. By regulating the carbonization temperature to acquire the target material with the optimum performance. To determine the carbon yield in lignite, thermogravimetric analysis (TGA) was conducted in an Ar atmosphere from 25 °C to 1000 °C at a rate of 10 °C min^{-1} (Fig. 4a). The thermal decomposition process of lignite can be divided into the following five stages [31,32]: (A) Dewater and Dry (25–120 °C). It mainly involves removing water from lignite. (B) Desorption of gases (120–200 °C). The adsorbed CO_2, CH_4, and N_2 in the lignite are desorbed. (C) Dehydroxylation reaction (200–360 °C). The carboxyl group in the organic acid molecule with the hydroxyl group in lignite is removed, generating CO_2. (D) Depolymerization and Decomposition (360–550 °C). The curve drops sharply, and a large number of volatile components of the primary product are released, including gases (methane, olefins, CO_2, CO, etc.) and tar. (E) Polycondensation (550–1000 °C). The main reaction involves the condensation of aromatic rings, leading to the release of significant quantities gases, including hydrogen, hydrocarbons, and carbon oxides. The volume of semi-coke shrinks, forming porous coke with cracks. The primary products undergo secondary cracking upon encountering high-temperature surfaces, giving rise to secondary products. X-ray diffraction (XRD) patterns of the three as-prepared samples reveal an amorphous structure with two broad peaks observed at approximately 23° and 44°, corresponding to (002) and (100) planes, respectively (Fig. 4b). As the temperature increases, the (002) peak shifts to a higher angle, indicating a decrease in the interlayer spacing of the carbon material. The interlayer distance of the three samples can be calculated using the Bragg equation. Specifically, the interlayer spacing of LC-1200 °C, LC-1400 °C, and LC-1550 °C is 0.389 nm, 0.385 nm, and 0.381 nm, respectively. The larger interlayer spacing is beneficial for the insertion and extraction of Na^+. The average width (La) of the graphite crystal along the a-axis direction and the thickness (Lc) of the graphite crystal along the c-axis direction are important parameters for describing caron crystallite, obtainable through the following equation:

$$L_{(nm)} = \frac{k\lambda}{\beta \cos\theta} \tag{3}$$

Where the constant k has a value of 1.84 for La and 0.89 for Lc, respectively, λ represents the wavelength of X-ray (0.154 nm), and β is the Full Width at Half Maxima (FWHM).

The values of La and Lc exhibit a growing trend from the LC-1200 °C to the LC-1500 °C, indicating that HTSP effectively adjusts the microstructure of the carbon material, subsequently impacting their sodium storage performance. The comparison of d_{002}, Lc, and La values for lignite-based carbon at different carbonization temperatures is illustrated in Fig. S13. According to the previously reported method [33], the R-value can serve as a characterization parameter for the degree of order in carbon materials. It can be obtained by measuring the ratio of the intensity of the (002) peak (B) to the background intensity (A) (Fig. S14 and Table S3). A higher R-value implies an increased degree of order in the carbon materials, which rises from 1.683 to 1.996 with the temperature increase, suggesting an enhancement in orderliness with elevated temperature. Raman spectroscopy is employed to analyze the defects and degree of graphitization in carbon materials. All samples exhibit a D peak

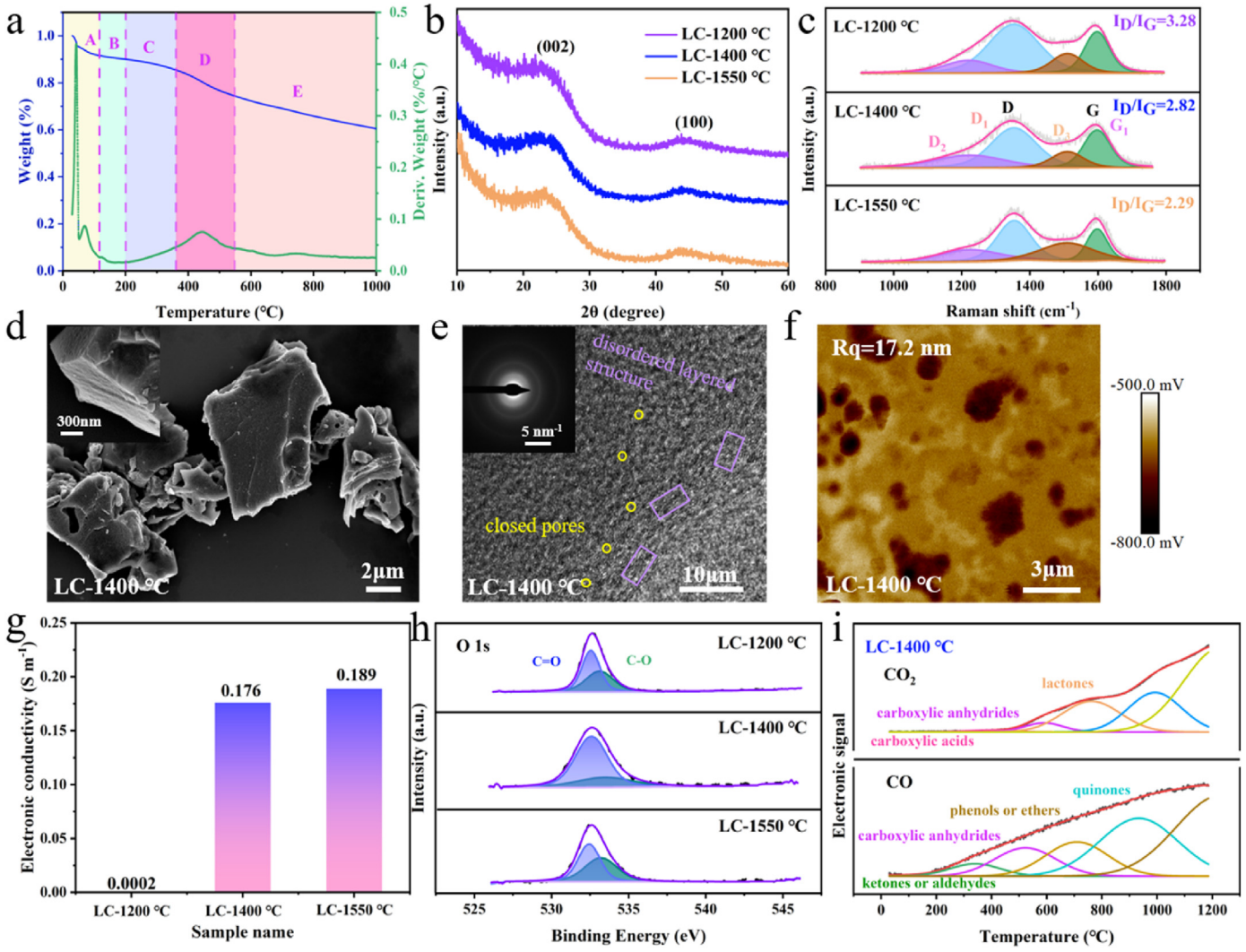

Fig. 4. (a) TGA of raw lignite. XRD patterns (b) and Raman spectra (c) for Lignite-based carbon at different carbonization temperatures. (d–f) Morphology characterizations of LC-1400 °C. SEM images (d), TEM images (Inset show the corresponding SAED patterns) (e), and AFM images (f). (g) Electronic conductivity and (h) high-resolution O 1s spectrum for three samples. (i) TG-MS of LC-1400 °C.

at ≈1340 cm^{-1} and a G peak at ≈1590 cm^{-1}, corresponding to the defects and crystalline nature of carbon materials, respectively (Fig. 4c). The peak of Raman spectra can be fitted into four sub-peaks at 1220 cm^{-1} (indicating the presence of alkenoid structure, amorphous carbon structure, and non-carbon heteroatoms), 1350 cm^{-1} (related to sp^3 hybridized carbon atoms and the disordered graphite lattice vibration mode at the edge of the graphite plane), 1510 cm^{-1} (arising from the amorphous carbon structure) and 1598 cm^{-1} (related to sp^3 hybridized carbon atoms and the stretching vibration of carbon atoms in the aromatic ring structure). The ID/IG ratio, obtained from the intensities of D and G peaks, serves as a measure of the graphitization degree of carbon materials. The ratio decreases from 3.28 for LC-1200 °C to 2.29 for LC-1550 °C, showing that the defects decrease and the graphitized degree increases. The XRD patterns and Raman spectra for the CSC are depicted in Fig. S15. Compared to LC-1400 °C, CSC has a relatively smaller d_{002} and I_D/I_G value, indicating narrow interlayer spacing and low defect concentration. The morphological and microcrystalline structures at different carbonization temperatures of the three samples using HTSP are characterized by scanning electron microscopy (SEM), high-resolution transmission electron microscopy (TEM), and corresponding selected area electron diffraction (SAED). All SEM images show distinct irregular layered structures (Fig. 4d, Figs. S16a–b). The TEM and SAED images reveal an amorphous structure in the carbon material, characterized by scattered diffraction rings (Fig. 4e and Figs. S16c–d). With increasing temperature, the locally ordered structures emerge due to the rearrangement of carbon atoms and the reduction of defects, resulting in enhanced graphite microcrystals. Simultaneously, the limited rearrangement of carbon microcrystals may lead to an increase in closed nano-pores, providing additional active sites for sodium ion storage, aligning well with the XRD and Raman results. Atomic Force Microscope (AFM) images and Kelvin Probe Force Microscopy (KPFM) assess the surface roughness of materials and the surface potential for lignite-derived carbon materials (Fig. 4f and Figs. S16e–f). The higher roughness of the LC-1200 °C may be attributed to its higher surface area, which is consistent with the results of BET surface area analysis. Smaller surface roughness can improve the interface contact between the anode electrode and electrolyte during the charging and discharging process, thereby enhancing long-term cycling performance [34]. The average surface potential values are −0.59, −0.62, and −0.68 V for LC-1200 °C, LC-1400 °C, and LC-1550 °C, respectively. The similarity in surface potential indicates comparable conductivity among these materials' surfaces. Electronic conductivity of the intrinsic material at room temperature is accurately determined using a Four probe resistivity tester (Fig. 4g). Electronic conductivity plays a crucial role in improving the charge transfer rate and the electrode rate performance. Notably, the electronic conductivity of lignite-derived carbon materials rapidly improves from 2×10^{-4} S m^{-1} to 0.189 S

m^{-1} as the temperature increases, underscoring the positive impact of enhanced graphitization on electronic conductivity. The surface chemical composition and state of lignite-based carbon materials with different carbonization times are examined using XPS spectroscopy (Fig. 4h and Fig. S17). The carbon contents for LC-1200 °C, LC-1400 °C, and LC-1550 °C are 86.7 %, 91.6 %, and 93.9 %, with corresponding oxygen contents of 13.3 %, 8.4 %, and 6.1 %, respectively. As the temperature increases, the carbon contents gradually increase while the oxygen contents gradually decrease. The C 1s spectra can be divided into four subpeaks at approximately 284.8, 285.3, 286.5, and 290 eV, corresponding to C-C sp^2, C-C sp^3, C-O, and C=O, respectively. The presence of defects, highlighted by the C-C sp^3 hybridization, is most concentrated in LC-1200 °C, as evidenced by Raman spectroscopy analysis. The O 1s spectra indicate the presence of oxygen-containing functional groups on the material surface, distinguishable into C=O (531.4 eV) and C-O (532.5 eV). The reversible reaction between C=O groups and Na^+ (C=O + Na^+↔C-O-Na) is relevant for sodium storage, correlated with the previous report. The higher contents of C=O groups in the LC-1400 °C compared to other carbon materials can enhance the rate performance of the carbon materials (Table S2) [35]. Given the limited detection depth of XPS, studying the oxygen functional groups (OFGs) on the surface of carbon materials can be challenging. Thermogravimetric mass spectrometry (TG-MS) can be used to analyze the thermal stability of OFGs by detecting the CO_2 and CO gases released during heating in an Ar atmosphere. By fitting the TG-MS peak area based on the decomposition temperature of functional groups, the content of OFGs can be calculated (Table S2) [36]. The CO_2 gas is mainly composed of carboxylic acid (150–450 °C), carboxylic anhydrides (300–650 °C) and lactones (600–800 °C). While the CO gas is mainly composed of ketones or aldehydes (200–400 °C), carboxylic anhydrides (400–650 °C), phenols, and ethers (600–800 °C), and quinones (750–1000 °C). Table S4 summarizes the relative content proportion of different OFGs. Among the carbon materials, the LC-1400 °C has the highest proportion of quinones and carboxylic anhydride functional groups. This makes it an ideal material for sodium storage, as these functional groups can facilitate the surface reaction kinetics by providing sites for C=O groups. Overall, the results indicate that moderate interlayer spacing, defect contents, and high C=O contents contribute to abundant sodium storage sites, promote the diffusion of sodium ions, and improve the rate performance of the lignite-derived carbon materials.

The pore structure evolution of carbonized materials at different temperatures significantly influences their electrochemical performance. We comprehensively characterized the pore structure of lignite-derived soft carbon (Fig. 5). The N_2 adsorption/desorption measurement is used to compare the Brunauer-Emmett-Teller (BET) surface area and pore diameter from open pores of the samples (Fig. 5a–b). The adsorption-desorption isotherms confirm the presence of graded porous structures with micropores and mesopores in all carbon materials, facilitating Na^+ adsorption and electrolyte permeation. As the temperature increases, the reduction of defects and the increase of ordered structures result in LC-1200 °C having higher surface defects with a specific surface area (SSA) of 88.5 m^2g^{-1}, while LC-1400 °C and LC-1550 °C exhibit relatively smaller SSA of 20.9 m^2 g^{-1} and 10.1 m^2 g^{-1}, respectively. The pore volume of the three samples at temperatures ranging from 1200 °C to 1550 °C are 0.0096, 0.016 and 0.02 cm^3 g^{-1}. The gradual increase in pore volumes indicates an incomplete formation of closed pores with an improvement in carbonization temperature. The adsorption of Na^+ on open pores is influenced by the SSA, and a larger SSA can lead to irreversible Na^+ consumption and electrolyte decomposition, unfavorable for high ICE. High temperatures induce carbon materials recombination and microcrystalline structure growth, transforming some open pores connected to the external environment into closed pores within the materials. These pore types exhibit distinct sodium storage mechanisms. BET analysis characterizes open pores, while small-angle X-ray scattering (SAXS) characterizes closed pores in the obtained samples (Fig. 5c). The SAXS patterns show an initial intensity drop and peaks at ≈0.05 $Å^{-1}$ [17], corresponding with a typical porous structure. A decrease in carbonization temperature leads to a less pronounced peak, suggesting a reduction in the radius of the closed

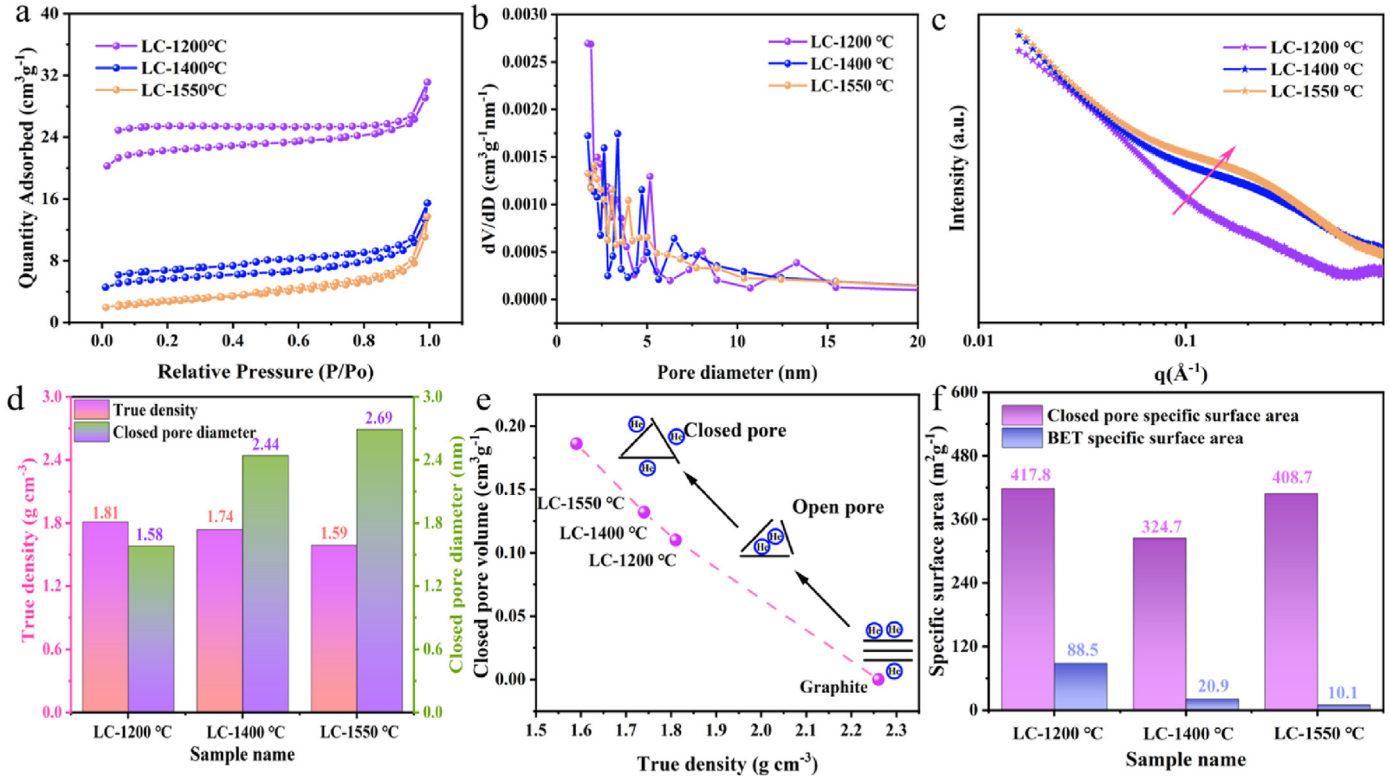

Fig. 5. N_2 adsorption-desorption isotherms (a), Pore diameter distribution (b), SAXS patterns (c), True density and closed pore diameter (d), True density and Closed pore volume(e), Closed pore specific area and BET specific area (f) of the three samples.

nanopores. By fitting the characteristic length associated with the variation of scattering power, the closed spherical radius can be calculated using the following two formulas:

$$I(q) = \frac{A}{q^a} + \frac{Ba_1^4}{(1 + a_1^2 q^2)^2} + D \tag{4}$$

$$R = a_1 \times 10^{1/2} \tag{5}$$

Where q represents the scattering vector, A and B are related to the total area of large and small pores, and D is a constant background term.

With increasing temperature, the closed pore diameter of the lignite-derived carbon materials measures 1.58, 2.44 and 2.69 nm, respectively. The capacity of carbon materials in the plateau region is closely connected to the volume of closed pores(Table S2) [37]. To accurately determine the skeleton density of carbon materials and obtain the closed pore volume of the test samples, the Archimedes principle-based true density test can be utilized as a supplementary tool to SAXS analysis. Since helium can enter almost all open nanopores except for closed ones, the true density test provides valuable information. Graphite, being the most compact material without closed pores, exhibits the highest true value of 2.26 g cm^{-3}(Table S2) [38]. Therefore, the closed pore volume of lignite-derived carbon materials can be calculated using 2.26 g cm^{-3} as the baseline, according to the following formula:

$$V_{Closed\ pore} = \frac{1}{\rho_{true}} - \frac{1}{2.26} \tag{6}$$

The true density value declines from 1.81 g to 1.59 cm^{-3} as the temperature rises (Fig. 5d and Table S5), while the closed pore volume increases from 0.11 to 0.186 $cm^3\ g^{-1}$ (Fig. 5e). These findings suggest that adjusting the carbonization temperature can effectively alter the pore structure of carbon materials and convert some open pores into closed pores. Additionally, assuming uniformly spherical pores for all closed pores, the SSA and quantity of closed pores can be determined (Fig. 5f and Table S5). Thus, the LC-1550 °C electrode exhibits the highest plateau capacity due to its larger closed volume, a significant factor in sodium storage in the plateau region.

3.5. Electrochemical performance of half-cell

The electrochemical performance of the lignite-derived carbon ma-

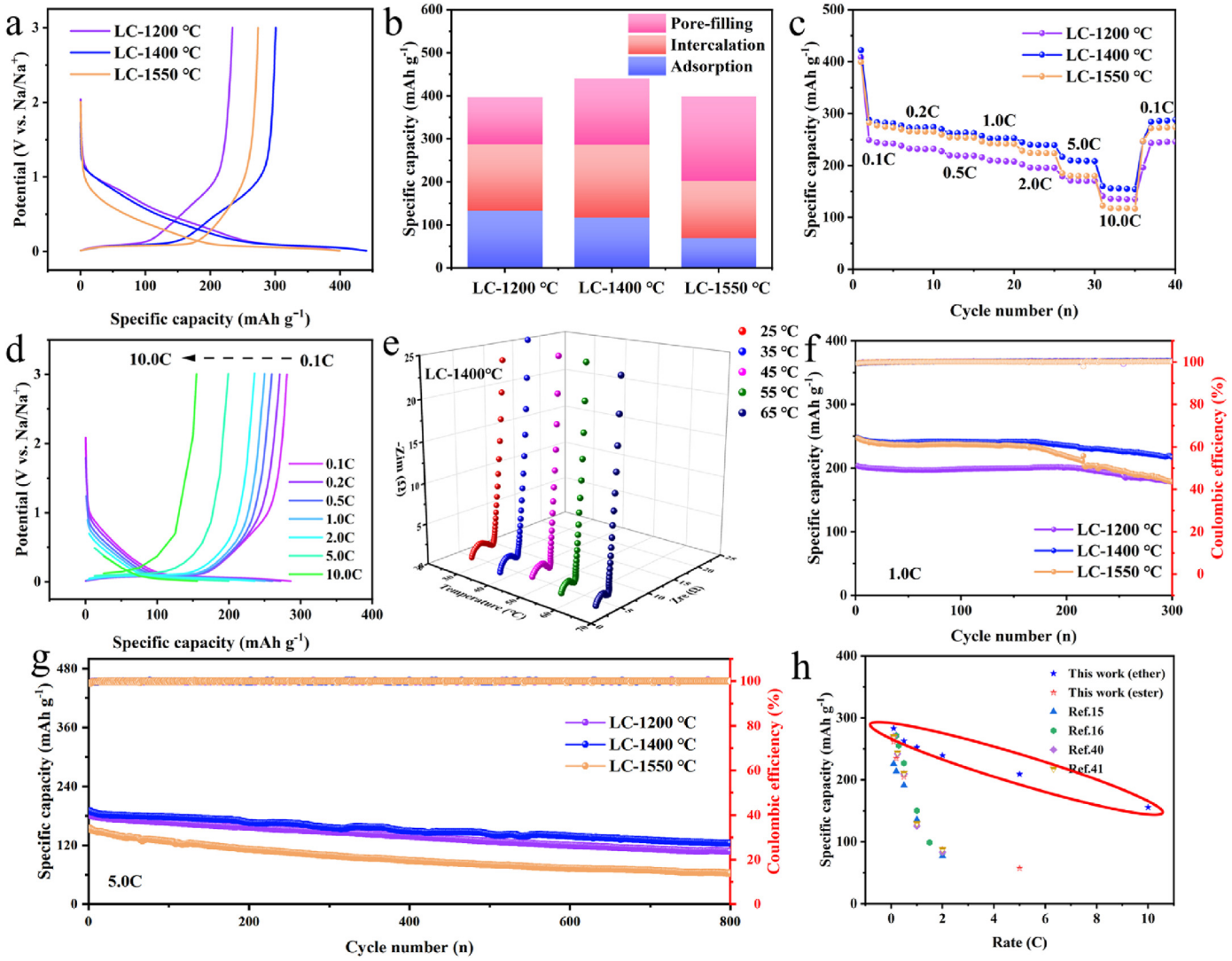

Fig. 6. (a–c) Comparison of half-cell electrochemical performance of the LC-1200 °C electrode, the LC-1400 °C electrode, and the LC-1550 °C electrode at 0.1C. The GCD curves in the potential range of 0.01–3.0 V (a). Specific capacity from the slope region, C=O, and plateau region contributions (b). Rate capability (c). (d) GCD profiles of the LC-1400 °C electrode at different current densities. (e) Nyquist plots at different temperatures for the LC-1400 °C electrode. (k) Comparison of room temperature capacity with the typical anodes reported previously.) (f–g) Comparison of Cycling performance of three samples. At the current density of 1.0C (f) and 5.0C (g). (h) The comparison of the LC-1400 °C electrode with previously reported coal-based materials [15,16,40,41].

terials is evaluated by Na carbon half-cells with 1M $NaPF_6$ diglyme electrolyte. The first GCD curves of the samples in the voltage range of 0.01–3.0 V (Fig. 6). All curves contain a slope region above 0.1 V and a plateau region below 0.1 V, representing surface adsorption and filling into the closed pores of Na-ion storage, respectively. Notably, a charge plateau at about 0.5 V is observed, attributing to the redox reaction between C=O and Na^+, as confirmed by ex situ XPS analysis. The initial discharge capacity and charge capacity of the LC-1400 °C electrode are 440.2 and 300.6 mAh g^{-1}, respectively, and the ICE is 68.3 %. In contrast, the LC-1200 °C electrode and the LC-1550 °C electrode exhibit initial discharge capacity and charge capacity of 397.3/234.2 mAh g^{-1} and 399.3/273.7 mAh g^{-1}, respectively, with ICE 58.9 % and 68.5 %. The low initial efficiency is attributed to SEI film formation and electrolyte decomposition during the first cycle. We provide several strategies to address the low ICE issue in supplementary information. The plateau capacity of the three carbon materials is 109.6, 153.7, and 196.6 mAh g^{-1}, while the slope capacity of the three carbon is 287.7, 286.5, and 202.7 mAh g^{-1}, among the slope region, the sodium storage of C=O is 155.0, 168.94, and 133.3 mAh g^{-1} (Fig. 6b), respectively. The LC-1550 °C electrode has the highest plateau capacity due to the highest closed pores. The LC-1200 °C electrode and the LC-1400 °C electrode have a similar slope capacity higher than the LC-1500 °C electrode, indicating the defects and the content of C=O groups jointly determine the sodium storage behavior in the slope region. The rate performance of the three samples is further studied with the current densities from 0.1C to 10.0 (Fig. 6c). As expected, the LC-1400 °C electrode exhibits highly reversible capacities of 160.0 mAh g^{-1} at the current densities of 10.0C, indicating its ultrafast Na^+ reaction kinetics. Fig. 6d illustrates the GCD curves of the LC-1400 °C electrode given to evaluate the electrochemical behavior at different current densities. As the current density rises, the capacity of the plateau region diminishes gradually, attributed to its slower kinetics compared to the slope region. The decay of total capacity is mainly caused by the decay of plateau region capacity, and balancing the capacity of the two regions is crucial for achieving high-rate SIBs. To delve into the kinetic behavior of sodium ions in detail, we conducted EIS and GITT analysis. The charge transfer kinetics are studied by Nyquist plots (Fig. S18). All the curves feature a straight line in the low-frequency region and a semicircle in the high and medium-frequency region, corresponding to Warburg diffusion resistance (W) and charge transfer resistance (Rst). The Rct value of the LC-1400 °C electrode is slightly lower than that of the LC-1200 °C electrode and LC-1550 °C electrode, demonstrating faster electronic transport kinetics. Moreover, the temperature-dependent EIS is further to study the Rct and activation energy (Ea) of the three samples in half-cell (Fig. 6e and Fig. S19). The Ea can be obtained from the Arrhenius equation. It can be found that the Ea for the LC-1400 °C electrode is smaller than that of the other electrodes, indicating that the unique structure of the LC-1400 °C electrode can accelerate the diffusion kinetics of Na^+ from the interface to the electrolyte, which is beneficial to the improvement of its high-rate performance. The GITT is employed to calculate the diffusion coefficient of Na^+, providing a valuable metric for assessing the storage kinetics behavior of Na^+ in electrode materials (Fig. 2d_3 and Fig. S20). The Na^+ diffusion coefficients can be calculated by the following formula:

$$D = \frac{4}{\pi\tau}\left(\frac{n_m V_m}{S}\right)^2\left(\frac{\Delta E_s}{\Delta E_t}\right)^2 \tag{7}$$

Where n_m, V_m, τ, and S are the mole of the electrode materials, molar volume, pulse duration, and surface area of the electrode, respectively.

The values of ΔE_s *and* ΔE_t can be obtained from the GITT curves (Fig. S5 and Fig. S20). All the electrodes exhibit similar diffusion behavior. The D_{Na+} values of the LC-1400 °C electrode (0.76×10^{-10} to 5.6×10^{-10}) show significant improvement compared to the LC-1200 °C electrode (0.64×10^{-10} to 4.5×10^{-10}) and the LC-1550 °C electrode (0.18×10^{-10} to 3.8×10^{-10}), correlating with the observed rate performance. In the 0.01–0.1 V range, the D_{Na+} of the discharge process slightly decreases at ≈0.06 V due to the slow kinetics of Na^+ filling into the closed pores, followed by a rapid decrease at ≈0.25 V due to the adsorption of a large number of sodium ions by electrode surface defects. To insert sodium ions into the interlayer composed of graphite microcrystals, it is necessary to overcome the repulsive force generated by sodium ions and surface defect sites. The rapid decrease of D_{Na+} in the slope region may be attributed to the formation of the SEI layer and the strong interaction between previously adsorbed Na^+ ions and the defect sites, hindering subsequent Na^+ cation adsorption and diffusion into the intercalation layer and closed pores. This explains the low initial efficiency of the carbon material and the reversible sodiation/desodiation behavior of sodium ions during the charging and discharging processes. The lignite-derived soft carbon not only exhibits superior rate performance but also possesses excellent cycling stability at both low and high current density. The capacity remains unchanged after 50 cycles at a current density of 0.1C (Fig. S21), while a 217 mAh g^{-1} reversible capacity with 87.8 % capacity retention can be achieved even at a density of 1.0C after 300 cycles for the LC-1400 °C electrode. This outperforms the LC-1200 °C electrode and LC-1550 °C electrode, which only exhibit a reversible capacity of 177.7 mAh g^{-1} with 87.3 % capacity retention and 176.6 mAh g^{-1} with 71.5 % capacity retention, respectively (Fig. 6f). To verify the cycling stability of the materials at high current density, the long-term cycling tests are conducted at a current density of 5.0C (Fig. 6g). The LC-1400 °C electrode still maintained a reversible capacity of 124 mAh g^{-1} with nearly 100 % coulombic efficiency after 800 cycles, comparable to hard carbon. Fig. 6h illustrates the outstanding rate performance of the LC-1400 °C electrode when compared to previously reported coal-based SIBs anode materials. Even in traditional ester electrolytes, the rate performance of the LC-1400 °C electrode rivals those reported in other literature. To our knowledge, there have been few reports on soft carbon for SIBs with such excellent sodium storage performance. The lignite-derived soft carbon stands out as a promising anode material for SIBs, demonstrating high capacity, superior cycling stability, and excellent rate performance, achieved through a simple and efficient method.

To clarify the superior performance of the LC-1400 °C electrode in the ether electrolyte, we compare it with testing in the ester electrolyte. As shown in Fig. S22a, the GCD curves in diglyme-based electrolytes at 0.1C are analogous to those in the EC/DMC-based electrolyte. However, differences emerge in the discharge curves between the two electrolytes at 1.0C (Fig. S22b). Compared to the LC-1400 °C electrode in diglyme-based electrolytes, the discharge curves plateau in EC/DMC-based electrolytes almost disappear, and the charge capacity sharply decreases, indicating slower kinetics in the EC/DMC-based electrolyte. Additionally, the LC-1400 °C electrode exhibits poor rate performance in EC/DMC-based electrolytes (Fig. S22c). At a current density of 5.0C, the specific capacity is 205.4 mAh g^{-1} in diglyme-based electrolytes, which is more than 3 times that in EC/DMC-based electrolytes (only 54.2 mAh g^{-1}). To understand the reasons behind the performance differences in the two electrolytes, further analysis is conducted from a kinetics perspective (Fig. S23). All EIS curves exhibit a semicircle in the high-frequency region and a straight line in the low-frequency region, indicating similar electrochemical reaction processes for the LC-1400 °C electrode at varied temperatures. The Rct in EC/DMC-based electrolytes is higher than that in diglyme-based electrolytes, suggesting a slower migration capability. By applying the Arrhenius equation, the Ea for the two different electrolytes is determined (Fig. S23c). Since the Rct is influenced by the de-solvation behavior, the Ea can be used to represent the de-solvation process of Na^+. The Ea of LC-1400 °C electrode in EC/DMC-based electrolyte is 30.68 kJ/mol, significantly higher than in diglyme-based electrolyte (10.02 kJ/mol), indicating the poor de-solvation ability of Na^+. Alters in morphology and structure greatly impact the performance of the battery during the cycling process (Fig. S24). After the first cycle, SEI is formed on the electrode surface in two electrolytes. After 50 cycles, the SEI in diglyme-based electrolyte becomes uniform, resulting in the formation of homogeneous porous

nanostructures on the electrode surface. This facilitates the electrolyte permeation and diffusion and alleviates the structural deformation during the Na^+ insertion/extraction processes. However, the SEI grows denser in EC/DMC-based electrolytes, hindering ion transport channels and possessing irreversible effects on electrochemical performance. Additionally, ex-situ XPS analysis of SEI composition is shown in Fig. S25. Results confirm stable sodium alkoxides (RCH_2ONa) and polyethers as the primary components in diglyme-based electrolytes, while destabilized alkyl-carbonates ($ROCO_2Na$) and polyester are the main constituents in EC/DMC-based electrolytes. The ($ROCO_2Na$) can decompose into Na_2CO_3 and RCH_2ONa, hindering Na^+ diffusion and producing unstable electrochemical interfaces(Table S2) [39]. This reduces the electrochemical kinetics of Na^+. Moreover, the activation energy affects the Na^+ diffusion rate through the SEI. The presence of NaF, an inorganic component in ether electrolyte, reduces the activation energy, whereas the organic component RCH_2ONa reduces the diffusion energy barrier of Na^+(Table S2) [40]. As a result, the rapid diffusion kinetics of lignite-derived soft carbon in diglyme-based electrolytes led to improved electrochemical performance in high-rate SIBs.

3.6. Sodium storage mechanism

A comprehensive analysis of the sodium storage mechanism is conducted using CV, ex-situ XPS, ex-situ XRD, ex-situ SAXS, and in-situ Rama (Fig. 7). The CV curves of the LC-1400 °C electrode are used to evaluate the sodium storage mechanism in the range of 0.01–3.0 V (Fig. 7a–b, Fig. S26). Fig. S26 shows the CV curves at 0.2 mV s^{-1} for three cycles. During the first discharging process, the irreversible oxidation peak occurs, which is attributed to the formation of SEI, irreversible reduction of oxygen-containing functional group, and decomposition of the electrolyte, leading to the generation of irreversible capacity. CV curves show a pair of redox peaks, with the curves nearly completely overlapping in the subsequent cycles, indicating outstanding reversibility in the insertion/extraction of Na^+ in the LC-1400 °C electrode. Furthermore, sodium-ion storage behavior is achieved by testing the CV curves at different scan rates from 0.2 to 1.0 mV s^{-1} (Fig. 7a) and it can be explained by the following equation:

$$i = av^b \tag{8}$$

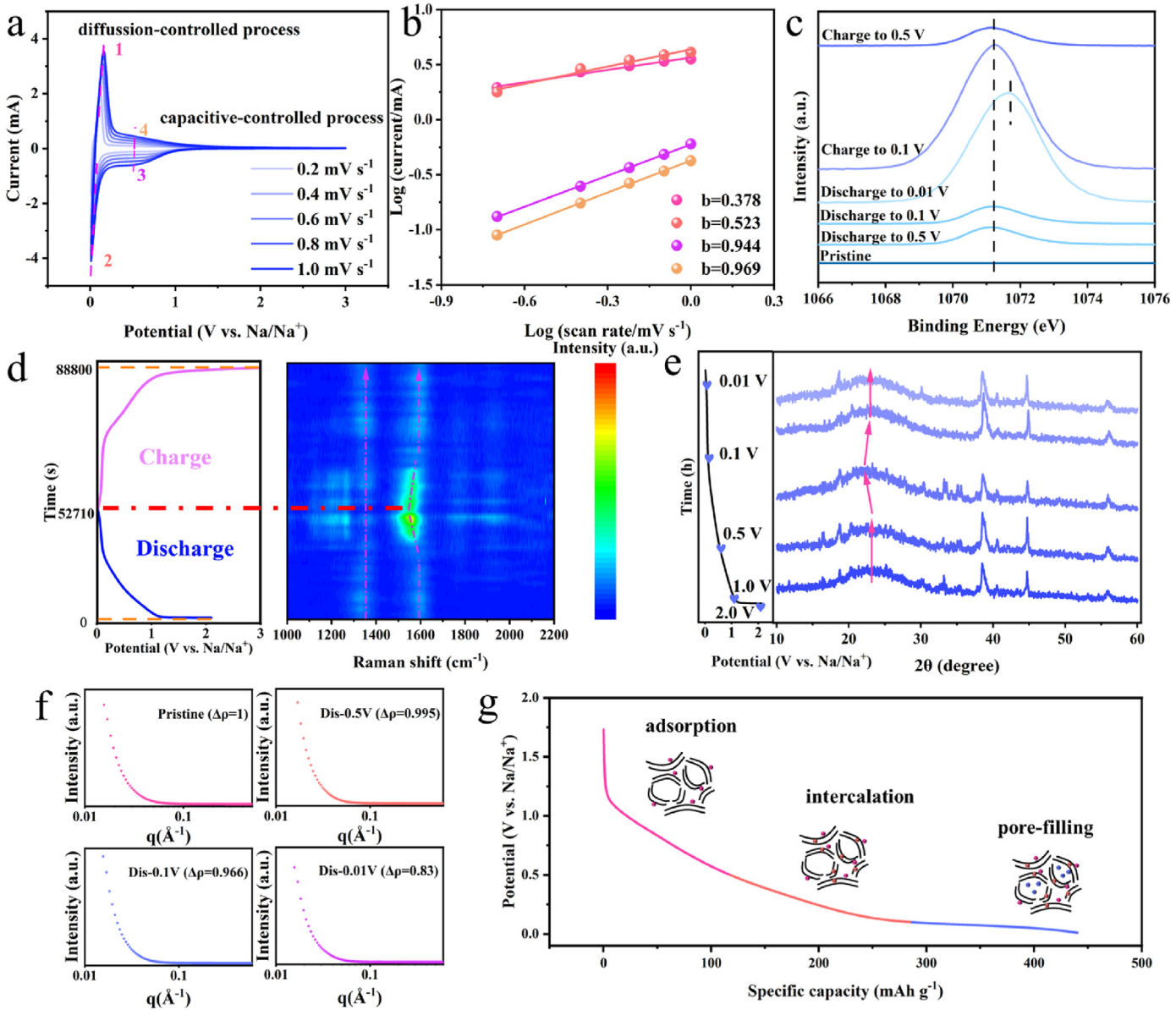

Fig. 7. The sodium-ion storage of the LC-1400 electrode. (a) CV curves at different scan rates from 0.2 mV s^{-1} to 1.0 mV s^{-1}. (b) Fitted plot of log (scan rate) versus log (current). (c) Ex-situ XPS Na 1s. (d) In-situ Raman. (e) Ex-situ XRD. (f) Ex-situ SAXS. (g) Scheme diagram of sodium-ion storage mechanism.

Where v is scanning rates, i is peak current, a and b are the constants.

The value of b is the slope of the log(v)-log(i) plot and can be used to reflect the electrochemical process. The value of b approaches 0.5 can be attributed to a diffusion-controlled process, while the b value close to 1 can be attributed to a capacitive-controlled process. As shown in Fig. 7b, the values of b for the LC-1400 °C electrode in the plateau region are 0.378 and 0.523, confirming a diffusion-controlled sodium storage process in the low-voltage region. On the contrary, the value of b in the slope region is 0.944, and 0.969 can be attributed to the capacitive-controlled process. In-situ and ex-situ tests can further authoritatively verify the sodium storage mechanism of the electrode by characterizing their structural evolution during the electrochemical reaction process. Ex-situ XPS is used to explore and detailed study the sodium storage behavior between C=O and Na^+ and the chemical bonding state of inserted Na in the LC-1400 °C electrode (Fig. 7c and Fig. S27). In Na 1s XPS spectra, a significant peak emerges at the binding energy of 1071.2 eV when the discharge voltage reaches 0.5 V, signifying successful Na^+ penetration into the carbon material. With further discharge, the position of the Na 1s peak does not shift. However, when the discharge reaches 0.01 V, the peak of Na 1s shifts to 1071.6 eV, which is closer to the binding energy of metallic sodium, indicating the absence of metallic sodium deposition and dendrites formation, consistent with the optical microscopy results. Upon charging to 0.1 V, the Na 1s returns to its original position, and with further charging to 0.5 V maintains the position nearly unchanged, indicating a highly reversible process. Meanwhile, considering that metallic bonds have a higher binding energy than surface adsorption, sodium is stored in a quasi-metallic state (pore-filling mechanism) in the platform region of the LC-1400 °C electrode material. As observed in Fig. S27, in O 1s XPS spectra, the intensity of C=O gradually decreases and the C-O-Na and Na KLL Auger gradually increase during the discharge process. Conversely, these trends reverse during the subsequent charge process. This phenomenon explains the reversible reaction between C=O and Na^+ to Na^+ storage, which is consistent with in situ Raman. In situ Raman spectrum (Fig. 7d), the voltage decreases from the open circuit to around 0.7 V, the G peak maintains constant, the intensity of D peak and the value of I_D/I_G gradually decreased, indicating that Na^+ adsorbed on the surface or defect sites of the electrode material. At the same time, when the discharge voltage reaches around 0.6 V, the G peak shifts to lower wavenumbers. This shift can be ascribed to the Na^+ insertion into the carbon layers, resulting in electron occupancy within the π* antibonding band. This occupation weakens the C-C bonds, subsequently resulting in a redshift of the G-band until the discharge voltage reaches 0.1 V. According to the previous, the formation of C-O-Na occurs through the reaction between C=O and Na^+ at ≈ 0.5–0.6 V. Additionally, during discharging to ≈0.01–0.1 V, the D peak disappears and the G peak exhibits no shift with the GITT analysis, confirming that Na^+ filling into the pores. The structural evolution of the electrode during the charging process is opposite to that discharge process, indicating excellent reversibility of sodiation/desodiation process. Ex-situ XRD of the LC-1400 °C electrode during the first discharge cycle at 0.1C is shown in Fig. 7e. Unlike the powder XRD, the impurity peaks arise in ex-situ XRD patterns due to the presence of electrolyte salt residue on the electrode surface. When the discharge voltage reaches 0.5 V, the (002) peak experiences a slight shift, returning to its original position when the discharge reaches 0.1 V. This observation further confirms Na^+ is embedded into the carbon layer around 0.5 V, consistent with in situ Raman date. Ex-situ SAXS is used to assess the electron density inside the closed pores of the LC-1400 °C electrode to further prove the pore-filling mechanism during the discharging process (Fig. 7f). The electron density contrast Δρ values at different sodiation states can be obtained based on the following modified Porod equation:

$$I(q) = \frac{A}{q^a} + \frac{Ba_1^6\Delta\rho^2}{\left(1+a_1^2q^2\right)^2} + \frac{C}{\left(1+a_2^2q^2\right)^2} + D \tag{9}$$

The Δρ denotes the variance in electron density between the closed pores and the surrounding carbon matrix. The electron density is set to 1 in the initial electrode.

The Δρ value in high voltage is almost the same as the pristine state in high voltage due to Na^+ primarily adsorbing on the electrode surface sites in the sloping region sodiation process. However, it declines after full sodiation, suggesting Na^+ filling into the closed pores of the electrode during the plateau sodiation process. Therefore, the sodium storage

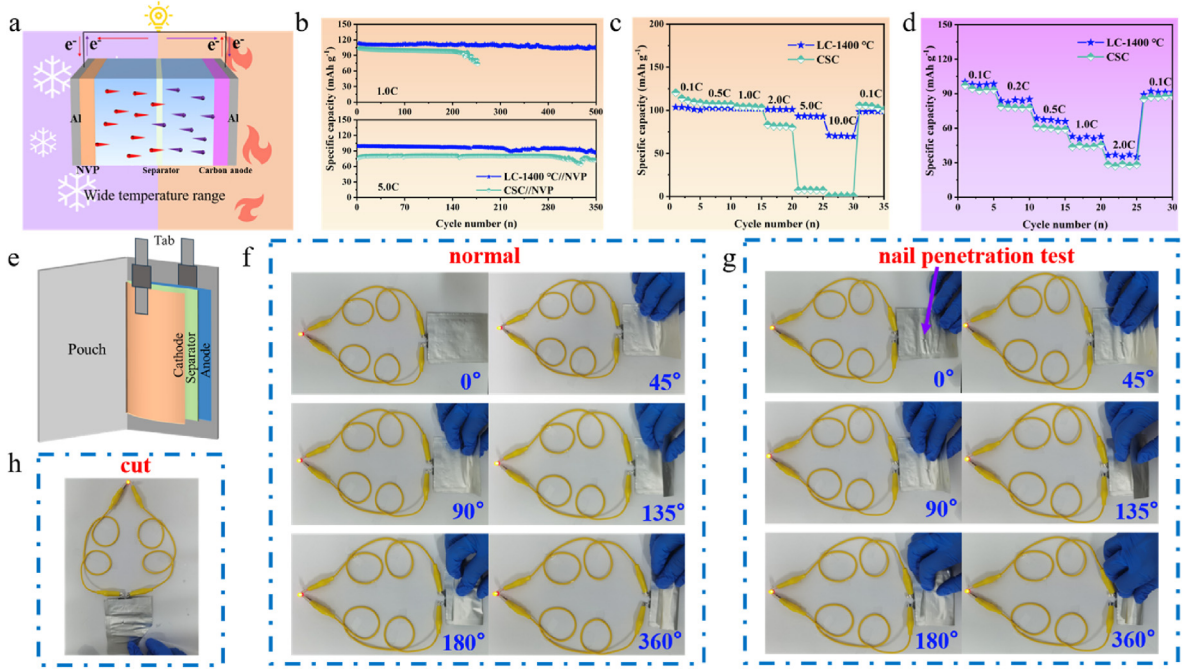

Fig. 8. (a–d) Electrochemical performance of carbon//NVP full-cell. (a) The schematic working mechanism of carbon//NVP full-cell at a wide temperature range. (b) Cycling stability of carbon//NVP full battery at 25 °C. (c, d) Comparison of rate capability at 25 °C (c) and −20 °C (d). (e–h) Pouch cell. (e) The schematic diagram for the sodium-ion pouch cell. (f–h) Digital images of the LEDs lightened by the pouch cell under different states.

mechanism of the LC-1400 °C electrode involves Na^+ adsorption on the surface or defect sites, insertion of Na^+ in the carbon layer, and the reaction between C=O and Na^+ in the slope region, as well as filling into closed pores in the plateau (Fig. 7g).

3.7. Electrochemical characterizations of the full-battery

To assess the practical applications of the LC-1400 °C electrode in the diglyme-based electrolyte, we construct a full battery using the LC-1400 °C electrode as the anode and pair it with the commercial $Na_3V_2(PO_4)_3$ (NVP) cathode (Fig. 8a). The full-cell tests are conducted at both −20 and 25 °C within a potential range of 2.0 V–3.8 V. The operating principle of the full-cell involves the movement of Na^+ from the NVP cathode to the LC-1400 °C anode, with electrons migrating in the same direction as the Na^+ in the external circuit during the charging process, and vice versa. The LC-1400 °C//NVP full battery demonstrates exceptional stability and high capacity retention. It maintains a discharge specific capacity of 103.9 mAh g^{-1} at 1.0C (1.0 C = 117 mA g^{-1}) with a capacity retention of 91.3 % over 500 cycles at 25 °C (Fig. S29). However, the capacity of the CSC//NVP full-cell decays relatively quickly after 200 cycles. Even at a high current density of 5.0C, the LC-1400 °C//NVP full battery outperforms the CSC//NVP full-cell, maintaining a capacity retention rate of 86.5 % after 350 cycles. Moreover, the LC-1400 °C//NVP full battery delivers an outstanding rate capability of 101, 93, and 71 mAh g^{-1} at the current densities of 2.0C, 5.0C, and 10.0C, respectively (Fig. 8c and Fig. S29). On the other hand, the CSC//NVP full battery exhibits a lower capacity of 81, 7, and 0 mAh g^{-1} at the same current densities (Fig. 8c). The significant difference in capacity, especially at high current densities, highlights the enormous application potential of the LC-1400 °C electrode in practical sodium energy storage. To address diverse application needs and enhance the adaptability of the full battery, it is crucial to investigate their performance in a wide temperature range. Comparative analyses at −20 °C, the LC-1400 °C//NVP full-cell consistently exhibits higher reversible capacity to the CSC//NVP full battery across all tested current densities, aligning with the room temperature findings (Fig. 8d). These exceptional properties of LC-1400 °C//NVP full-cell make the LC-1400 °C electrode a promising candidate for commercial SIBs anode material. Its stability and remarkable capacity retention, even at high current densities, demonstrate its potential for practical energy storage applications. Finally, the pouch cell is fabricated to explore safety and more practical applications in flexible energy storage devices, as depicted in Fig. 8e. Owing to the excellent flexibility and high safety of the LC-1400 °C electrode, the pouch cell can light LED bulbs under normal conditions and withstand nail penetration after different bending angles (Fig. 8f and g). Even when cut into pieces, the LEDs can still be lit (Fig. 8h). Based on the total mass of anode and cathode active material, the energy density of the LC-1400 °C electrode is 235.8 Wh kg^{-1} with a high discharge voltage platform of 3.363 V. Therefore, the LC-1400 °C holds significant potential as a flexible electrode for SIBs. Further research and development are needed to optimize its properties and enhance its performance for commercialization.

4. Conclusions

We elaborately design an environmentally friendly and cost-effective method to synthesize high-rate anode materials for SIBs from lignite via an ultrafast and efficient high-temperature thermal shock pulse approach. The rapid Na^+ diffusion, high electron/ion transfer capacity, excellent desolvation ability, and low interfacial impedance inhibit dendrite growth, imparting splendid electrochemical properties to the electrode materials. The optimized sample displays excellent reversible capacity at 0.1C (176.2 mAh g^{-1}@-40 °C, 300.6 mAh g^{-1}@25 °C, 706.8 mAh g^{-1}@80 °C) and superior rate performance at 5.0C (71.7 mAh g^{-1}@-20 °C, 205.4 mAh g^{-1}@25 °C and 62.2 mAh g^{-1}@60 °C), outperforming the state-of-the-art literature. More importantly, the assembled full-cell delivers stable cycle performance (103.9 mAh g^{-1} at 1.0C after 500 cycles and 86.1 mAh g^{-1} at 5.0C after 350 cycles) and decent rate capacity at 25 °C (70.5 mAh g^{-1}@10.0C) and −20 °C (35.2 mAh g^{-1}@2.0C). Hence, this work provides a simple and efficient new technique for the precise regulation of soft carbon anode materials for SIBs in a wide temperature range. We believe this strategy can serve as a universal approach for designing high-performance carbon anode materials.

CRediT authorship contribution statement

Ru Wang: Writing – review & editing, Writing – original draft, Visualization, Investigation. **Yiming Fan:** Software. **Jiaqi Wang:** Writing – review & editing. **Yuyang Li:** Data curation. **Xiangyang Li:** Validation. **Feng Jin:** Software. **Xiaofei Hu:** Writing – review & editing.

Declaration of competing interest

The authors declare no competing financial interest.

Acknowledgements

This work was supported by the National Natural Science Foundation of China (No. 52201278) and the Young Talent Support Plan of Xi'an Jiaotong University (for X. F. H.). The authors acknowledge the Department of Science and Technology of Shaanxi Province (QCYRCXM-2022-126).

Appendix A. Supplementary data

Supplementary data to this article can be found online at https://doi.org/10.1016/j.pnsc.2024.11.002.

References

[1] R. House, U. Maitra, M. Pérez-Osorio, J. Lozano, L. Jin, J. Somerville, L. Duda, A. Nag, A. Walters, K. Zhou, M. Roberts, Superstructure control of first-cycle voltage hysteresis in oxygen-redox cathodes, Nature 577 (2022) 502–508.
[2] Y. Li, X. Lu, X. Zhao, H. Wang, X. Hu, Recent advances in research on cathodes for low-temperature sodium-ion batteries, Prog. Nat. Sci.: Mater. Int. 33 (2023) 767–779.
[3] R. Wang, S. Zhang, S. Peng, Y. Tong, X. Hu, Research progress of electrolyte additives for subzero-temperature aqueous sodium-ion batteries, Carb. Neutrality. 3 (2024) 6.
[4] H. Fang, Y. Huang, W. Hu, Z. Song, X. Wei, J. Geng, Z. Jiang, H. Qu, J. Chen, F. Li, Regulating ion-dipole interactions in weakly solvating electrolyte towards ultra-low temperature sodium-ion batteries, Angew. Chem. Int. Ed. 63 (2023) e202400539.
[5] X. Lu, S. Li, Y. Li, F. Wu, C. Wu, Y. Bai, From lab to application: challenges and opportunities in achieving fast charging with polyanionic cathodes for sodium-ion batteries, Adv. Mater. 36 (2024) 2407359.
[6] E. Gabriel, C. Ma, K. Graff, A. Conrado, D. Hou, H. Xiong, Heterostructure engineering in electrode materials for sodium-ion batteries: recent progress and perspectives, eScience 3 (2023) 100139.
[7] Y. Li, Y. Guo, K. You, C. Guo, C. Li, X. Zeng, W. Wang, Q. Tang, Y. Yuan, Porous bismuth nanocrystals with advanced sodium ion storage property, Prog. Nat. Sci.: Mater. Int. 33 (2023) 92–99.
[8] Z. Song, G. Zhang, X. Deng, K. Zou, X. Xiao, R. Momen, A. Massoudi, W. Deng, J. Hu, H. Hou, G. Zou, X. Ji, Ultra-low-dose pre-metallation strategy served for commercial metal-ion capacitors, Nano-Micro Lett. 14 (2022) 53.
[9] Z. Song, G. Zhang, X. Deng, Y. Tian, X. Xiao, W. Deng, H. Hou, G. Zou, X. Ji, Strongly coupled interfacial engineering inspired by robotic arms enable high-performance sodium-ion capacitors, Adv. Funct. Mater. 32 (2022) 2205453.
[10] B. Xin, X. Wu, Research progresses on metal-organic frameworks for sodium/potassium-ion batteries, Battery Energy (2024) 20230074.
[11] X. Xiao, X. Duan, Z. Song, X. Deng, W. Deng, H. Hou, R. Zheng, G. Zou, X. Ji, High-throughput production of cheap mineral-based heterostructures for high power sodium ion capacitors, Adv. Funct. Mater. 32 (2022) 2110476.
[12] J. Amouroux, P. Siffert, J. Massué, S. Cavadias, B. Trujillo, K. Hashimoto, P. Rutberg, S. Dresvin, X. Wang, Carbon dioxide: a new material for energy storage, Prog. Nat. Sci.: Mater. Int. 24 (2014) 295–304.
[13] M. Li, W. Tsai, B. Thapaliya, H. Meyer, B. Armstrong, H. Luo, S. Dai, J. Nanda, I. Belharouak, Modified coal char materials with high rate performance for battery applications, Carbon 172 (2021) 414–421.
[14] R. Li, B. Yang, A. Hu, B. Zhou, M. Liu, L. Yang, Z. Yan, Y. Fan, Y. Pan, J. Chen, T. Li, Heteroatom screening and microcrystal regulation of coal-derived hard carbon promises high-performance sodium-ion batteries, Carbon 15 (2023) 118489.

[15] Y. Li, Y. Hu, X. Qi, X. Rong, H. Li, X. Huang, L. Chen, Advanced sodium-ion batteries using superior low cost pyrolyzed anthracite anode: towards practical applications, Energy Storage Mater. 5 (2016) 191–197.
[16] K. Wang, F. Sun, H. Wang, D. Wu, Y. Chao, J. Gao, G. Zhao, Altering thermal transformation pathway to create closed pores in coal-derived hard carbon and boosting of Na^+ plateau storage for high-performance sodium-ion battery and sodium-ion capacitor, Adv. Funct. Mater. 32 (2022) 2203725.
[17] Y. Dong, S. Yuan, W. Zhao, C. Yi, Z. Zeng, S. Xie, Y. Yang, W. Sun, X. Ji, P. Ge, Tailoring natural anthracite carbon materials towards considerable electrochemical properties with exploration of ester/ether-based electrolyte, J. Mater. Chem. A 11 (2023) 9668–9681.
[18] Y. Wang, N. Xiao, Z. Wang, H. Li, M. Yu, Y. Tang, M. Hao, C. Liu, Y. Zhou, J. Qiu, Rational design of high-performance sodium-ion battery anode by molecular engineering of coal tar pitch, Chem. Eng. J. 342 (2018) 52–60.
[19] K. Wang, J. Qian, F. Sun, Z. Tian, J. Gao, G. Zhao, In-situ catalytic conversion of coal pyrolysis gas to nanoporous carbon rods and superior sodium ion storage performance, Fuel 281 (2020) 118782.
[20] N. Xiao, Y. Wei, H. Li, Y. Wang, J. Bai, J. Qiu, Boosting the sodium storage performance of coal-based carbon materials through structure modification by solvent extraction, Carbon 162 (2020) 431–437.
[21] H. Zhao, D. Zhao, J. Ye, P. Wang, M. Chai, Z. Li, Directional oxygen functionalization by defect in different metamorphic-grade coal-derived carbon materials for sodium storage, Energy Environ Mater 5 (2022) 313–320.
[22] H. Chen, N. Sun, Y. Wang, R. Soomro, B. Xu, One stone two birds: pitch assisted microcrystalline regulation and defect engineering in coal-based carbon anodes for sodium-ion batteries, Energy Storage Mater. 56 (2023) 532–541.
[23] S. Liu, Y. Shen, Y. Zhang, B. Cui, S. Xi, J. Zhang, L. Xu, S. Zhu, Y. Chen, Y. Deng, W. Hu, Extreme environmental thermal shock induced dislocation-rich Pt nanoparticles boosting hydrogen evolution reaction, Adv. Mater. 34 (2022) 2106973.
[24] C. Wang, W. Ping, Q. Bai, H. Cui, R. Hensleigh, R. Wang, A. Brozena, Z. Xu, J. Dai, Y. Pei, C. Zheng, G. Pastel, J. Gao, X. Wang, H. Wang, J. Zhao, B. Yang, X. Zheng, J. Luo, Y. Mo, B. Dunn, L. Hu, A general method to synthesize and sinter bulk ceramics in seconds, Science 368 (2020) 521–526.
[25] Y. Yao, Q. Dong, A. Brozena, J. Luo, J. Miao, M. Chi, C. Wang, I. Kevrekidis, Z. Ren, J. Greeley, G. Wang, High-entropy nanoparticles: synthesis-structure-property relationships and data-driven discovery, Science 376 (2022) 3103.
[26] X. Zhou, Z. Li, W. Li, X. Li, J. Fu, L. Wei, H. Yang, X. Guo, Regulating Na-ion solvation in quasi-solid electrolyte to stabilize Na metal anode, Adv. Funct. Mater. 33 (2023) 2212866.
[27] Z. Chang, H. Yang, Y. Qiao, X. Zhu, P. He, H. Zhou, Tailoring the solvation sheath of cations by constructing electrode front-faces for rechargeable batteries, Adv. Mater. 34 (2022) 2201339.
[28] X. Hu, E. Matios, Y. Zhang, C. Wang, J. Luo, W. Li, Deeply cycled sodium metal anodes at low temperature and in lean electrolyte conditions, Angew. Chem. Int. Ed. 60 (2021) 5978–5983.
[29] M. Doyle, T. Fuller, J. Newman, Modeling of galvanostatic charge and discharge of the lithium/polymer/insertion cell, J. Electrochem. Soc. 140 (1993) 1526.
[30] T. Gao, Y. Han, D. Fraggedakis, S. Das, T. Zhou, C. Yeh, S. Xu, W. Chueh, J. Li, M. Bazant, Interplay of lithium intercalation and plating on a single graphite particle, Joule 5 (2021) 393–414.
[31] T. Qin, Q. Lu, H. Xiang, X. Luo, Y. Fu, Ca promoted Ni–Co bimetallic catalyzed coal pyrolysis and char steam gasification, Energy 82 (2023) 128374.
[32] S. Liu, H. Zhao, X. Liu, Y. Li, G. Zhao, Y. Wang, M. Zeng, Effect of hydrothermal upgrading on the pyrolysis and gasification characteristics of baiyinhua lignite and a mechanistic analysis, Fuel 276 (2020) 118081.
[33] J. Yang, X. Wang, W. Dai, X. Lian, X. Cui, W. Zhang, K. Zhang, M. Lin, R. Zou, K. Loh, Q. Yang, From micropores to ultra-micropores inside hard carbon: toward enhanced capacity in room-/low-temperature sodium-ion storage, Nano-Micro Lett. 13 (2021) 1–14.
[34] Z. Zhang, S. Said, K. Smith, R. Jervis, C. Howard, P. Shearing, D. Brett, T. Miller, Characterizing batteries by in situ electrochemical atomic force microscopy: a critical review, Adv. Energy Mater. 11 (2021) 2101518.
[35] Z. Song, M. Di, S. Chen, Y. Bai, Three-dimensional N/O co-doped hard carbon anode enabled superior stabilities for sodium-ion batteries, Chem. Eng. J. 470 (2023) 144237.
[36] D. Zhao, H. Zhao, J. Ye, W. Song, S. Miao, H. Shen, Y. Zhao, M. Kang, Z. Li, Oxygen functionalization boosted sodium adsorption-intercalation in coal based needle coke, Electrochim. Acta 329 (2020) 135127.
[37] Y. Li, A. Vasileiadis, Q. Zhou, Y. Lu, Q. Meng, Y. Li, P. Ombrini, J. Zhao, Z. Chen, Y. Niu, X. Qi, Origin of fast charging in hard carbon anodes, Nat. Energy 9 (2024) 134–142.
[38] L. Ji, Y. Zhao, L. Cao, Y. Li, C. Ma, X. Qi, Z. Shao, A fundamental understanding of structure evolution in the synthesis of hard carbon from coal tar pitch for high-performance sodium storage, J. Mater. Chem. A 11 (2023) 26727–26741.
[39] Y. Liang, N. Song, Z. Zhang, W. Chen, J. Feng, B. Xi, S. Xiong, Integrating Bi@ C nanospheres in porous hard carbon frameworks for ultrafast sodium storage, Adv. Mater. 34 (2022) 2202673.
[40] M. Liu, F. Wu, Y. Gong, Y. Li, Y. Li, X. Feng, Q. Li, C. Wu, Y. Bai, Interfacial-catalysis-Enabled layered and inorganic-rich SEI on hard carbon anodes in ester electrolytes for sodium-ion batteries, Adv. Mater. 35 (2023) 2300002.
[41] H. Chen, N. Sun, Y. Wang, R. Soomro, B. Xu, One stone two birds: pitch assisted microcrystalline regulation and defect engineering in coal-based carbon anodes for sodium-ion batteries, Energy Storage Mater. 56 (2023) 532.